RSC Advances

PAPER

View Article Online
View Journal | View Issue

Cite this: *RSC Adv.*, 2025, **15**, 23783

Icariin delivery system based on covalent organic framework materials: dual effects of immune modulation and osteogenesis promotion

Mingdong Luo,†[ab] Xueqing Lin,†[ab] Na Wang,[c] Qishan Xie,[abde] Shiyi Zeng,[ab] Shiting Li,*[ab] Zhoukun He *[de] and Xiaorong Lan *[abfg]

Bone defects, induced by trauma, infection, tumor resection, osteoporosis, and congenital deformities, severely affect patient health both physiologically and psychologically, imposing substantial burdens on healthcare systems and public resources. Bone defect repair involves a complex biological process that orchestrates events such as immune modulation and osteogenic differentiation. Consequently, ideal materials for bone defect regeneration should possess capabilities in both immune regulation and osteogenesis. In this study, we synthesized a kind of covalent organic framework (COF) nanoparticles at room temperature and modified their surface with polydopamine (PDA), resulting in PDA-functionalized COFs (PCOFs). Utilizing the adhesive properties of PDA, we successfully loaded icariin (ICA) onto the PCOFs nanoparticles, forming ICA@PCOFs. Comprehensive characterization techniques, including visual inspection, scanning electron microscopy (SEM), Fourier-transform infrared spectroscopy (FTIR), and thermogravimetric analysis (TGA), confirmed the successful synthesis of ICA@PCOFs nanoparticles. Subsequent optimal concentration determination *via* the CCK-8 assay, and further experiments including alkaline phosphatase (ALP) activity, alizarin red S (ARS) staining, and immunofluorescent staining for osteocalcin (OCN), runt-related transcription factor 2 (Runx2), inducible nitric oxide synthase (iNOS), and mannose receptor (CD206), assessed their capability to modulate macrophage polarization and promote osteogenesis. The results revealed that ICA-loaded nanoparticles demonstrated significant potential *in vitro* for immune regulation and promoting stem cell osteogenic differentiation. These findings suggest that ICA@PCOFs nanoparticles could represent a promising therapeutic platform for bone defect regeneration, offering dual functionalities in immune modulation and osteogenesis promotion.

Received 19th February 2025
Accepted 2nd July 2025

DOI: 10.1039/d5ra01207d

rsc.li/rsc-advances

1. Introduction

Bone defects, caused by trauma, infection, tumor removal, osteoporosis, and congenital deformities, significantly impact patients' physiological and psychological health and impose a substantial burden on healthcare systems and public resources.[1] Research data indicates that the global market for bone grafts and substitutes was valued at $3.16 billion in 2024, with projections suggesting an increase to $4.4 billion by 2030.[2] This data underscores that the repair of bone defects has become a major public health challenge globally, necessitating the development of more effective treatment methods and solutions.

Traditionally, autologous bone grafting has been regarded as the gold standard for bone defect repair.[3] However, its limitations cannot be overlooked.[4] Autologous bone is usually harvested from the iliac crest or fibula, resulting in limited donor availability, which makes it challenging to meet the demands of large-scale bone defect repair. Additionally, the bone harvesting procedure not only subjects patients to additional surgical trauma but also increases the risk of complications such as donor site bleeding and infection, further complicating the recovery process. In recent years, with the introduction of new technologies and concepts in the fields of materials science, biology and medicine, bone tissue engineering has made remarkable progress and gradually become one of the most promising alternatives in the field of bone defect repair.[5]

[a]*Luzhou Key Laboratory of Oral & Maxillofacial Reconstruction and Regeneration, The Affiliated Stomatological Hospital of Southwest Medical University, Luzhou, 646000, China. E-mail: xiaoronglancdm@163.com; tingtinghigh@sina.com; Tel: +86 18384297885; +86 18623127651*

[b]*Basic Medicine Research Innovation Center for Cardiometabolic Diseases, Ministry of Education, Southwest Medical University, Luzhou, 646000, China*

[c]*Shandong Huayu University of Technology, Dezhou, 253000, China*

[d]*School of Mechanical Engineering, Chengdu University, Chengdu, 610106, China. E-mail: hezhoukunhe@163.com; Tel: +86 18224407693*

[e]*Research Center of Composites & Surface and Interface Engineering, Chengdu University, Chengdu, 610106, China*

[f]*Institute of Stomatology, Southwest Medical University, Luzhou, 646000, China*

[g]*Metabolic Vascular Diseases Key Laboratory of Sichuan Province, Southwest Medical University, Luzhou, Sichuan, 646000, China*

† These authors contributed equally to this work.

However, the repair of bone defects is a complex biological process that involves a finely coordinated interplay of immune regulation, osteogenic differentiation, and other biological events.[6] During this process, various cellular and molecular mechanisms must be precisely coordinated to ensure effective repair and functional restoration of bone tissue. Therefore, ideal materials for bone defect regeneration should possess multifunctional capabilities, not only supporting cell adhesion, proliferation, and differentiation but also facilitating immune modulation and accelerating bone regeneration. The combination of these functions can effectively improve the local microenvironment at the bone defect site, enhance the effectiveness of the repair, and overcome the limitations of existing treatment methods, especially in the repair of complex bone defects.

Icariin (ICA) is the main active component of the traditional Chinese herb Epimedium. It is a light yellow acicular crystalline powder with various biological activities, including immune modulation[7] and osteogenesis promotion, and is widely used in the field of bone defect repair.[8,9] Firstly, ICA can modulate immune responses by inhibiting the reactive oxygen species (ROS)-dependent JNK/NF-κβ signaling pathway, significantly reducing the mRNA expression of classic pro-inflammatory factors such as tumor necrosis factor-α (TNF-α), interleukin-6 (IL-6), and interleukin-8 (IL-8) induced by lipopolysaccharide (LPS).[10–12] This immune modulation is particularly crucial for bone defect repair in chronic inflammatory conditions like diabetes. Secondly, in bone defect repair, ICA promotes osteoblastic differentiation and bone matrix formation by inducing the expression of osteogenic genes such as alkaline phosphatase (ALP), runt-related transcription factor 2 (Runx2), osteocalcin (OCN), and type I collagen, thereby accelerating the repair and regeneration of bone defects.[13–15] Thirdly, ICA also regulates the osteoprotegerin/nuclear factor-κβ ligand (OPG/RANKL) pathway, inhibiting the activity of osteoclasts and reducing bone resorption, which is particularly important for patients with metabolic bone disorders like diabetes, who often suffer from increased bone resorption and decreased bone density.[16] By balancing bone resorption and formation, ICA helps improve bone quality and facilitate the repair of bone defects.[17] In summary, the role of ICA in bone defect repair extends beyond promoting osteogenesis; it also creates an optimal environment for bone regeneration through its immune-modulatory effects. Thus, ICA holds significant potential in bone tissue engineering, especially in treating bone defects associated with diabetes, due to its extensive therapeutic properties.

Covalent organic frameworks (COFs) are an emerging class of porous crystalline polymers constructed *via* covalent bonds between light elements (*e.g.*, C, H, O, N, B).[18,19] Representative examples include COF-1 and COF-5, based on boronic acid linkages, and TpPa-1, based on Schiff base chemistry, all of which exhibit high surface area, regular pore channels, and tunable functionality.[20,21] In the field of bone defect repair, the application of COFs as biomedical materials has received extensive attention in recent years, largely due to their outstanding properties: ease of functionalization, high surface area, excellent thermal and chemical stability, and good biocompatibility.[22] Bhunia S. *et al.* synthesized a stable two-dimensional hydrolysable COF which they found could effectively induce osteogenic differentiation in human mesenchymal stem cells (HMSCs) through osteogenesis induction experiments.[23] Building on this, they utilized its porous structure to successfully load the osteogenesis promoter dexamethasone, achieving sustained drug release and significantly enhancing the osteoinductive capability of bone implants. These studies have laid the foundation for the application of COF-based drug delivery systems in bone defect repair, demonstrating their enormous potential as an innovative strategy for bone tissue regeneration.

Polydopamine (PDA) is a mussel-inspired biomimetic material that can form through the self-polymerization of dopamine molecules in a mildly alkaline environment. Due to its abundance of catechol and primary and secondary amine groups, PDA exhibits strong adhesive properties, enabling it to widely adhere to various solid surfaces, making it extensively used for interfacial modification of materials.[24] Moreover, in bone defect repair, PDA-modified nanomaterials not only enhance biocompatibility but also regulate inflammatory responses and oxidative stress in the body, providing a more favorable microenvironment for the affected area.[25] PDA modification allows for further functionalization of COFs surfaces, achieving more precise drug release control and optimizing the local bone regeneration environment.[26] Additionally, PDA-modified nanomaterials can improve interactions between the materials and biological molecules such as bone cells and stem cells, promoting cell attachment, proliferation, and differentiation, thus accelerating the repair process of bone defects.[27] Therefore, combining the dual advantages of COFs and PDA to develop functionalized drug delivery systems represents an innovative treatment strategy in the field of bone defect repair, offering more efficient and precise support for bone regeneration.

This study aims to develop a multifunctional material for bone defect repair, specifically a delivery system based on COFs material loaded with ICA. As shown in Fig. 1, we first synthesized COFs nanoparticles at room temperature and then modified their surfaces through the self-polymerization reaction of dopamine to produce PDA-modified COFs (PCOFs). Utilizing the strong adhesive properties of catechol and amine groups in PDA molecules, we successfully loaded ICA onto the PCOFs nanocarriers, creating a multifunctional bone filler (ICA@PCOFs) with dual immune modulation and osteogenic effects. The proposed ICA@PCOFs multifunctional bone filler, combining the high surface area and porous structure of COFs with the surface functionalization properties of PDA, is expected to achieve effective loading and sustained release of ICA, thereby accelerating bone regeneration while modulating immune responses. Through a series of *in vitro* experiments, including cell viability assays, anti-inflammatory factor expression analysis, and evaluation of osteogenic differentiation markers, the material's effects on immune modulation and osteogenesis promotion were systematically validated. This innovative strategy offers a new therapeutic approach for bone

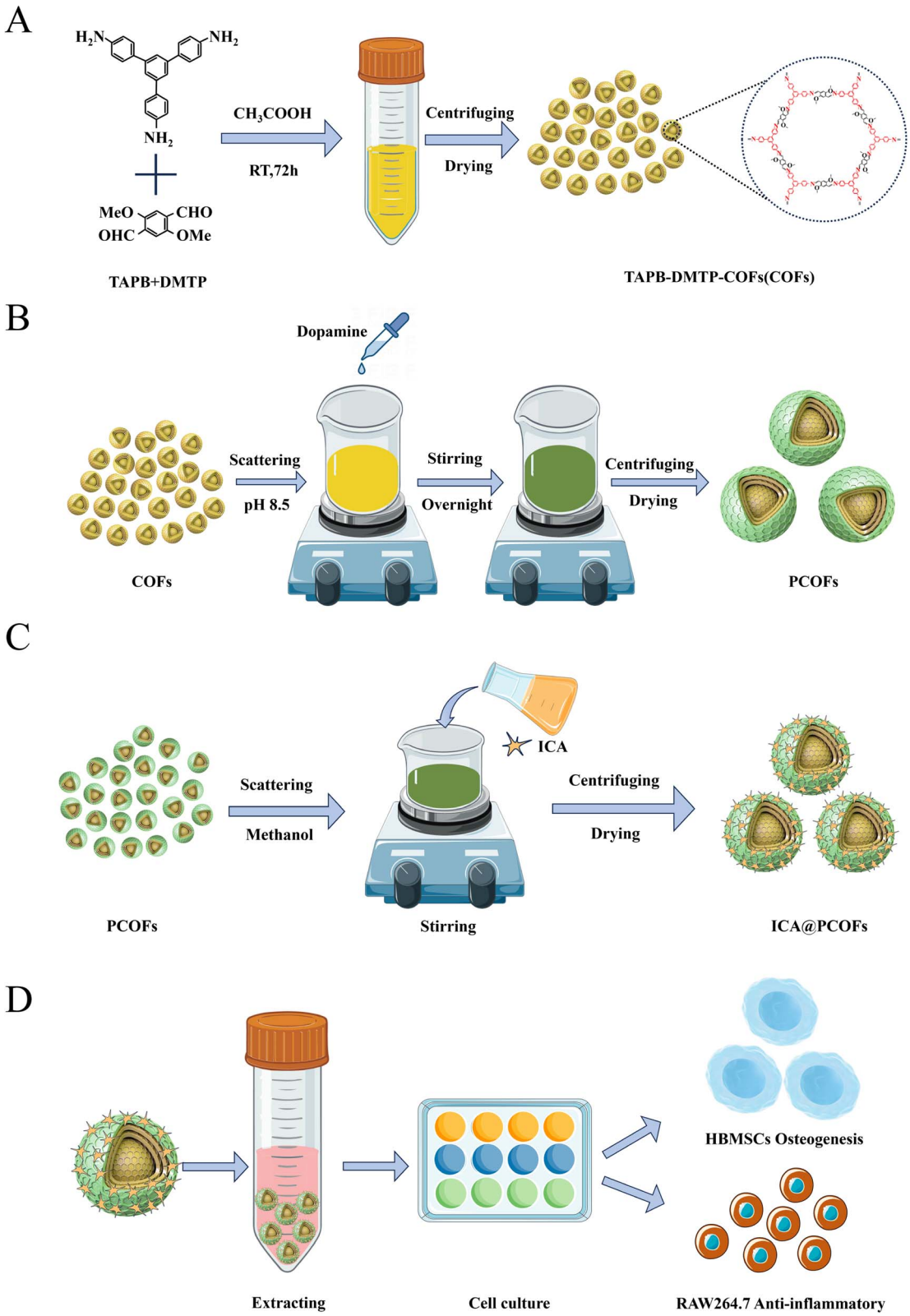

Fig. 1 Schematic illustration of the preparation and *in vitro* testing of ICA@PCOFs: (A) synthesis of COFs; (B) synthesis of PCOFs; (C) synthesis of ICA@PCOFs; (D) *in vitro* validation of ICA@PCOFs.

defect repair, holding broad potential applications in the field of bone regeneration.

2. Materials and methods

2.1 Materials

1,3,5-Tris(4-aminophenyl)benzene (TPB) and 2,5-dimethoxyterephthalaldehyde (DMTP) were purchased from Jilin Zhongke Yanshen Technology Co., Ltd (Jilin, China). Tetrahydrofuran (THF), acetonitrile (CAN), acetic acid (HOAc), ethyl acetate (EA) and methanol (MeOH) were purchased from Chengdu Kelong Chemical Co., Ltd (Sichuan, China). Dopamine hydrochloride was acquired from Shanghai Aladdin Biochemical Technology Co., Ltd (Shanghai, China). Tris–HCl buffer was obtained from Shanghai Saint-Bio Biotechnology Co., Ltd (Shanghai, China). ICA was bought from Beijing Solarbio Science & Technology Co., Ltd (Beijing, China). Human bone marrow mesenchymal stem cells (HBMSCs), the macrophage line RAW 264.7, and alizarin red S (ARS) staining solution were purchased from Cyagen Biosciences Inc. (Guangzhou, China). BCIP/NBT ALP Chromogenic Kit was obtained from Beyotime Biotechnology Co., Ltd (Shanghai, China). CCK8 assay kit was purchased from Beijing Labgic Technology Co., Ltd (Beijing, China). Osteocalcin (OCN) and Runx2 antibodies were sourced from Abcam Trading (Shanghai) Co., Ltd (Shanghai, China). Inducible nitric oxide synthase (iNOS) and mannose receptor (CD206) antibodies were acquired from Proteintech Group, Inc. (Hubei, China). Goat Anti-Rabbit IgG/Alexa Fluor® 594 was purchased from ZSGB-BIO Biotechnology Co., Ltd (Beijing, China).

2.2 Synthesis of ICA@PCOFs

2.2.1 Preparation and characterization of COFs. At room temperature, monomers TPB 35.1 mg and DMTP 29.1 mg were weighed into a 50 mL centrifuge tube. Under ultrasound, 16 mL CAN was added as the solvent, and the monomer was completely dissolved by ultrasound for 10 min. Then 1 mL of HOAc was added as the catalyst, and the ultrasound was continued for 10 min. Reaction at room temperature for 72 h. After the reaction, the mixture was eluted with THF for three times, and the yellow precipitation was obtained by 6000 rpm centrifugation. Yellow powdered COFs were obtained after drying at 40 °C, −0.02 MPa and vacuum for 12 h. The COFs materials were characterized using X-ray diffraction (XRD; Malvern Panalytical X'Pert^3, Netherlands), scanning electron microscopy (SEM; FEI Ispect F50, USA), surface area analysis (BET; Micromeritics 3Flex, USA), thermogravimetric analysis (TGA; Rigaku TG-DTA 8121, Japan), and Fourier-transform infrared spectroscopy (FTIR; Thermo Fisher Scientific Nicolet iS 10, USA) to determine the crystallinity, surface morphology, surface area, pore size, thermal stability, and functional group structure.

2.2.2 Preparation and characterization of PCOFs. 50 mg of COFs are weighed and ultrasonically dispersed in 20 mL of Tris buffer solution (10 mM, pH 8.5). Additionally, 20 mg of dopamine hydrochloride is dissolved in 5 mL of deionized water and slowly added to the COFs–Tris suspension under magnetic stirring at 400 rpm. The reaction is allowed to proceed at room temperature for 24 hours, resulting in a PCOFs suspension. The suspension is dialyzed for 24 hours using an 8–12 kDa dialysis bag with a ratio of reaction liquid to deionized water of 1 : 200. The product is collected by centrifugation at 8000 rpm for 30 minutes. Finally, the product is dried under vacuum at 50 °C and −0.06 MPa for 8 hours to obtain PCOFs powder. The successful grafting of PDA is confirmed by SEM, TGA, and FTIR analyses.

2.2.3 Preparation and characterization of ICA@PCOFs

2.2.3.1 ICA loading. 50 mg of PCOFs are weighed and ultrasonically dispersed in 20 mL of MeOH. Additionally, 20 mg of ICA is dissolved in 20 mL of MeOH by ultrasonication, and the ICA–MeOH solution is slowly added to the PCOFs–MeOH suspension under magnetic stirring at 500 rpm. The reaction is allowed to proceed at room temperature for 24 hours, resulting in an ICA@PCOFs suspension. The suspension is washed three times with 20 mL of MeOH and the product is collected by centrifugation at 8000 rpm for 10 minutes. Finally, the product is dried under vacuum at 40 °C and −0.02 MPa for 12 hours to obtain ICA@PCOFs powder. The powder is weighed and recorded, and the experiment is repeated three times. The average yield of ICA@PCOFs is calculated based on the mean of the three results, with an average yield of 53.3 mg. The successful loading of ICA is confirmed by SEM, TGA, and FTIR analyses.

2.2.3.2 The drug loading content (DLC) and encapsulation efficiency (EE) of ICA. ICA standard curve preparation: 5 mg of ICA standard is precisely weighed and placed into a 50 mL round-bottom flask. An adequate amount of MeOH is added to fully dissolve the ICA, and the solution is brought up to 50 mL to prepare a 100 μg mL^{-1} ICA MeOH stock solution. Precise aliquots of this stock are taken and diluted with MeOH to prepare standard solutions of 50, 25, 12.5, 6.25, and 3.13 μg mL^{-1}. MeOH serves as the blank control. The absorbance of each solution is measured at 270 nm using a UV-vis spectrophotometer (PERSEE T700A, China). The absorbance is plotted against the ICA concentration, and a linear regression equation is obtained for the ICA standard solutions.

The DLC and EE of ICA: 5 mg of ICA@PCOFs powder is precisely weighed and dispersed in 20 mL of MeOH. The solution is sonicated for 2 hours to release the drug, followed by centrifugation at 8000 rpm for 10 minutes to collect the supernatant. The supernatant is filtered through a 0.22 μm membrane, and the absorbance of the filtrate is measured at 270 nm using a UV-vis spectrophotometer. The ICA concentration is calculated based on the regression equation of the ICA standard curve. The DLC and EE of ICA@PCOFs were calculated using the following formulas:

$$\mathrm{DLC}\ (\%) = W_0/W_\mathrm{D} \times 100\%$$

where W_0 is the mass of ICA encapsulated in ICA@PCOFs (μg), and W_D is the total mass of ICA@PCOFs (μg).

$$\mathrm{EE}\ (\%) = W_0 \times 100\%/W_\mathrm{E}$$

where W_0 is the mass of ICA encapsulated in ICA@PCOFs (μg), and W_E is the total mass of ICA initially added during the preparation of ICA@PCOFs (μg).

2.2.3.3 The cumulative release (CR) of ICA in vitro. A total of 5 mg of ICA@PCOFs was immersed in 50 mL of phosphate-buffered saline (PBS) and placed in a 37 °C incubator to investigate the *in vitro* release behavior of ICA. At 1, 3, 5, 7, and 14 days, 1 mL of PBS was collected and replaced with an equal volume of fresh PBS. The collected PBS samples were extracted three times with an equal volume of EA. The organic phase was then evaporated using a rotary evaporator and redissolved in an equal volume of methanol. The absorbance of the resulting solution was measured at 270 nm using a UV-vis spectrophotometer (PERSEE T700A, China), and the concentration of ICA was calculated based on the ICA standard curve.

The CR of ICA from ICA@PCOFs was calculated using the following equation:

$$\mathrm{CR}\ (\%) = (V_0 \times C_t + V \times \sum C_i)/M \times 100\%$$

where V_0 is the total volume of the release medium (mL), C_t is the concentration of ICA in the release medium at the final time point (μg mL^{-1}), V is the volume withdrawn at each sampling time point (mL), C_i is the ICA concentration at each previous time point (μg mL^{-1}), M is the total mass of ICA loaded in ICA@PCOFs (μg).

2.3 Biocompatibility of ICA@PCOFs

Biocompatibility testing was conducted using HBMSCs. All experiments involving HBMSCs were approved by the Institutional Review Board of the Affiliated Stomatological Hospital of Southwest Medical University (approval number: 20241104014). ICA@PCOFs powder was soaked in α-MEM (Gibco, USA) basic medium (1 mg mL^{-1}) for 48 hours, centrifuged, and filtered through a 0.22 μm filter to obtain the ICA@PCOFs extract. Subsequently, 10% fetal bovine serum (FBS; Gemini, Australia) + 1% penicillin–streptomycin (Hyclone, USA) were added to prepare complete culture medium at various concentration gradients (1000, 500, 100, 10, and 1 μg mL^{-1}). HBMSCs were seeded into 96-well plates at 800 cells per well (100 μL per well) and cultured for 24 hours. Afterward, the original medium was replaced with the complete culture medium containing different concentration gradients of extracts and further cultured for 24, 72, and 120 hours. 10 μL of CCK-8 solution was added and incubated in a culture incubator for 1 hour. The optical density (OD) at 450 nm was measured using an enzyme-linked immunosorbent assay reader (Agilent, Synergy HTX, USA). Bar charts were drawn, and data were analyzed. Images were also collected using an inverted phase contrast microscope (Olympus CKX53, Japan). Based on the results of the CCK8 assay, suitable concentrations of PCOFs and ICA@PCOFs extracts (same concentration for both) were selected for subsequent immunomodulatory effects and osteogenesis experiments.

2.4 Immunomodulatory effects of ICA@PCOFs

2.4.1 Experimental groups. The experiments were divided into four groups. The negative control group was only cultured with normal medium (control group), and the positive control group was stimulated with LPS (100 ng mL^{-1}) for 24 hours and then cultured with normal medium for 24 hours (LPS group). The experiment group 1 was cultured with PCOFs extract for 24 hours after LPS stimulation (LPS + PCOFs group), while the experiment group 2 was cultured with ICA@PCOFs extract for 24 hours after LPS stimulation (LPS + ICA@PCOFs group).

2.4.2 Immunofluorescence staining of iNOS and CD206. The cell slides were placed in a 24-well plate, and Raw 264.7 was inoculated into the plate at a density of 4×10^4 cells per well, and the corresponding treatment was carried out according to different groups 24 hours later. After treatment, cells were fixed with 4% paraformaldehyde solution at 4 °C for 15 minutes, permeabilized with 0.5% Triton X-100, and blocked with 5% goat serum (Solarbio, China) for 1.5 hours. Overnight incubation with primary antibodies (1 : 400) against iNOS and CD206 followed. Cells were then incubated with secondary antibodies (1 : 200) for 1 hour. Finally, DAPI stain was added, and the cells were incubated in the dark for 15 minutes. Fluorescence expression of iNOS and CD206 was observed using a fluorescence microscope, and semi-quantitative analysis of fluorescence intensity was performed using Image J.

2.5 Osteogenesis of ICA@PCOFs

2.5.1 Experimental groups. The experiment was divided into three groups. The control group was the osteogenic induction medium group (Os-Blank), the experiment 1 group was the PCOFs osteogenic induction group (Os-PCOFs), and the experiment 2 group was the ICA@PCOFs osteogenic induction group (Os-ICA@PCOFs). The induction medium consists of 10% FBS, 1% penicillin–streptomycin, 50 mg L^{-1} ascorbic acid (Macklin, China), 10 mM β-glycerophosphate sodium (Macklin, China), 100 nmol L^{-1} dexamethasone (Macklin, China), and the respective extracts (PCOFs and ICA@PCOFs extracts).

2.5.2 ALP staining. HBMSCs were seeded at a density of 4×10^4 cells per well in a 12-well plate. Once confluence reached 80%, the medium was replaced with the corresponding osteogenic induction medium. The medium was changed every 3 days. After 7 days of culture, the medium was removed, and the cells were rinsed with PBS, fixed with 4% paraformaldehyde at 4 °C for 30 minutes, then washed three times with PBS. Subsequently, cells were stained with prepared BCIP/NBT ALP staining solution and images were captured under a microscope.

2.5.3 ARS staining. The cultivation procedure is the same as described in Section 2.5.2. After 14 days of culture, cultivation was terminated, cells were fixed with 4% paraformaldehyde solution, and stained with ARS solution at room temperature for 15 minutes. The staining solution was discarded, and cells were repeatedly rinsed with deionized water. The mineralization nodules in the extracellular matrix were observed under a microscope, and images were captured.

2.5.4 Immunofluorescence staining of OCN and Runx2. Cell slides were placed in a 24-well plate, and HBMSCs were seeded at a density of 2×10^3 cells per well. After 24 hours, the medium was replaced with corresponding induction medium and cells were treated for 5 days. Then, the medium was

removed, and the cells were rinsed with PBS and fixed with 4% paraformaldehyde at 4 °C for 15 minutes. Membrane permeabilization was performed using 0.5% Triton X-100 for 15 minutes. After rinsing with PBS, cells were blocked with goat serum blocking solution (consisting of 10% goat serum, 1% bovine serum albumin (Solarbio, China), 0.3 M glycine (Macklin, China) and 0.1% Tween 20 (Solarbio, China)) for 1.5 hours. Freshly prepared primary antibodies against OCN and Runx2 were then added, and the cells were incubated overnight at 4 °C in the dark. The next day, after rewarming, the primary antibodies were removed, and secondary antibodies were added for protein labeling staining. Nuclei were stained with DAPI solution, followed by rinsing with PBS. Finally, the cell slides were removed, inverted onto a slide with anti-fluorescent quenching agent, edges sealed with nail polish, and images were captured using an upright fluorescence microscope (Olympus, Japan). Semi-quantitative analysis was performed using Image J software.

2.6 Statistics analysis

All data are presented as mean ± standard deviation. Differences between two groups were analyzed using independent sample *t*-tests, while differences among more than two groups were analyzed using one-way ANOVA. Statistical analyses were performed using SPSS 21 software, and $p < 0.05$ was considered statistically significant.

3. Results and discussion

3.1 Preparation and characterization of ICA@PCOFs

3.1.1 Physicochemical properties of ICA@PCOFs. The structural and physicochemical properties of the COFs were systematically investigated using a suite of characterization techniques. Combined analytical approaches confirmed the successful construction of the covalent organic framework with defined crystallinity and porosity. Fig. 2A presents the XRD pattern of the COFs. A strong peak is observed at 2.79°, and medium intensity peaks appear at 4.82°, 5.56°, and 7.38°, with a weak peak at 9.70°. These diffraction features are consistent with those reported previously for TAPB–DMTP based COFs in the literature.[28,29] Fig. 2B shows the BET analysis results of the COFs. The pore size is observed to be approximately 2.3 nm, and the specific surface area is about 930 $m^2 g^{-1}$. Compared to the values reported in previous literature (pore size of 3.3 nm and specific surface area of 2400 $m^2 g^{-1}$),[30] the values obtained in this study are smaller. This is primarily attributed to the synthesis of COFs at room temperature in this study, which led to poorer crystallinity and consequently smaller BET specific surface area and pore size. In Fig. 2C, the FTIR spectrum of COFs shows peaks at 1287 cm^{-1} corresponding to the stretching vibrations of C–O, at 1464 cm^{-1} attributed to the asymmetric stretching vibrations of $-CH_3$, and at 1592 cm^{-1} associated with the bending vibrations of $-NH_2$. Furthermore, the TGA results of COFs in Fig. 2D, the physical appearance in Fig. 2E, the SEM morphology in Fig. 2F, and the particle size analysis results in Fig. 2G are consistent with those reported in the literature.[28–31] These data indicate that TAPB–DMTP based COFs has been successfully synthesized.

Furthermore, we modified COFs with PDA in order to obtain PCOFs. In the FTIR spectrum of PCOFs shown in Fig. 2C, a broader and stronger absorption peak was observed in the range of 3200–3700 cm^{-1} due to the association of hydroxyl and amino groups from the abundant catechol and primary and secondary amines in PDA with the characteristic peaks of COFs. This indicates that PDA was successfully grafted onto the COFs.[32,33]

Following the chemical confirmation of PDA grafting through FTIR analysis, we further explored the macroscopic and microscopic transformations induced by this surface modification. The structural evolution was manifested through distinct alterations in optical properties, morphological features, and colloidal behavior. In Fig. 2E, a comparison of the physical appearance of COFs and PCOFs revealed that the color of the COFs nanoparticles changed from yellow to dark green after grafting with PDA. Fig. 2F and G show that, as compared to COFs, the surface morphology of PCOFs transitioned from smooth to rough, and their average diameter significantly decreased from 443.43 ± 60.24 nm to approximately 228.28 ± 28.44 nm. This reduction in size may be attributed to a thin layer of PDA formed on the COFs' surface, which is believed to act as a stabilizing shell that could promote better dispersion of the particles in solution, leading to a more uniform distribution of particles.[34] These results confirm that PDA was successfully grafted onto the surface of COFs, resulting in the successful acquisition of PCOFs.

Finally, leveraging the strong adhesive properties of PDA, ICA was intended to be loaded onto the surface of PCOFs. From the FTIR spectrum, as compared to PCOFs, new peaks were observed on ICA@PCOFs at 1654 cm^{-1} corresponding to the C=C stretching vibrations and at 1260 cm^{-1} for the C–O stretching vibrations, indicating that ICA was successfully loaded onto the surface of PCOFs.[35]

Having established the chemical anchoring of ICA through FTIR characterization, we proceeded to validate the composite's structural integrity and thermal behavior through complementary analytical methods. The thermogravimetric profiles coupled with morphological evolution provided multidimensional verification of successful drug loading. In the TGA analysis, the curves of PCOFs and COFs were found to be essentially consistent, with 92% mass remaining at 389 °C, indicating good thermal stability for both. In contrast, the thermal degradation of pure ICA was characterized by a rapid weight loss at 241 °C, dropping from 99% to 26% by 389 °C, demonstrating that ICA begins to degrade at 241 °C. The TGA curve of ICA-loaded PCOFs showed a similar trend of significant mass reduction at 241 °C, but returned to a trend similar to that of COFs and PCOFs by 389 °C, further confirming the successful loading of ICA. At the same time, visual observation of the physical photographs revealed that the color of PCOFs nanoparticles changed from dark green to yellow-green after loading ICA. SEM results indicated that the diameter of ICA-loaded PCOFs increased from 228.28 ± 28.44 nm to 247.14 ± 23.96 nm. These

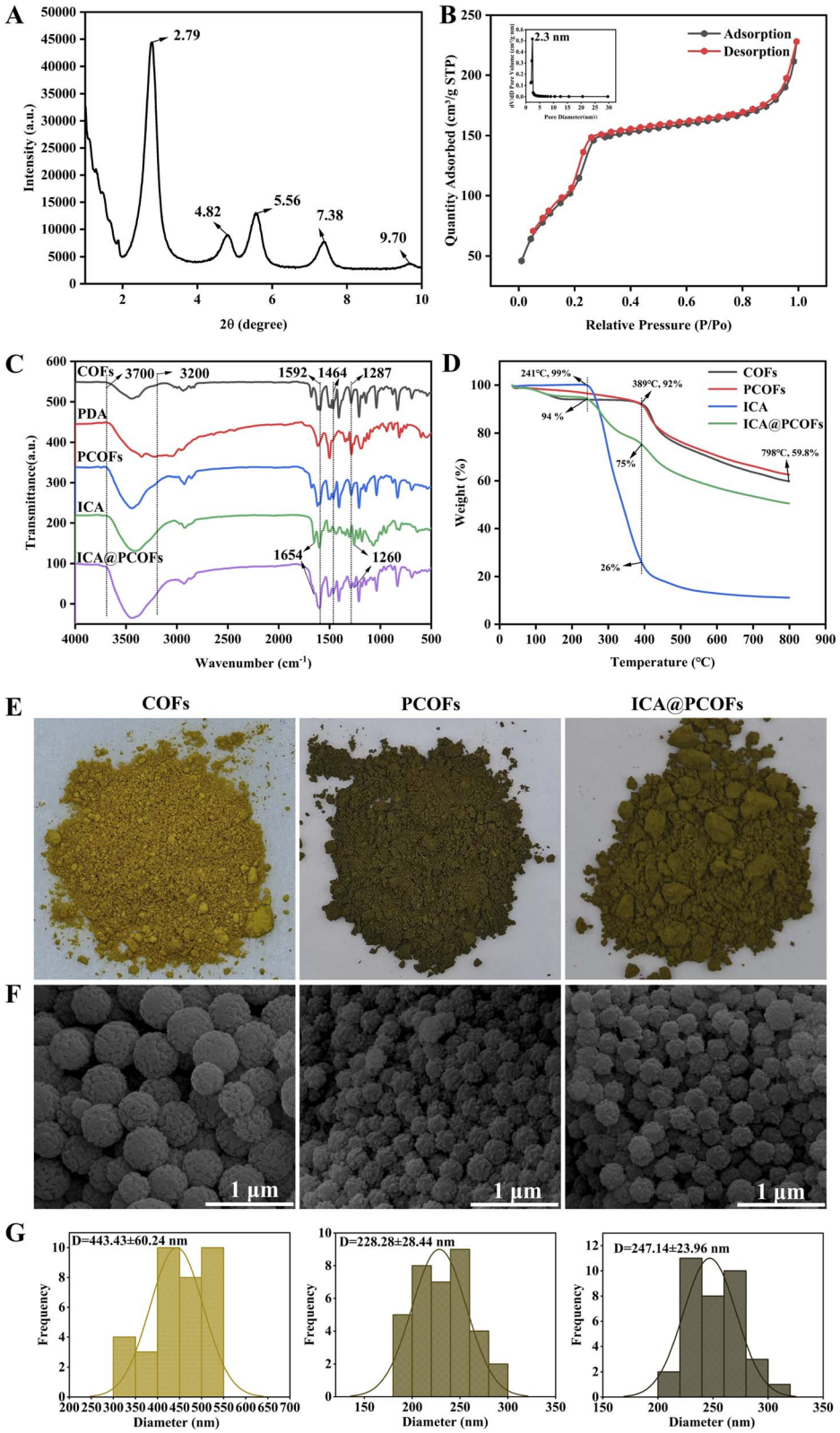

Fig. 2 Physicochemical characterization results of COFs, PCOFs, and ICA@PCOFs: (A) XRD results of COFs; (B) BET results of COFs; (C) FTIR results of COFs, PCOFs, and ICA@PCOFs; (D) TGA results of COFs, PCOFs, and ICA@PCOFs; (E) physical optical photographs of COFs, PCOFs, and ICA@PCOFs; (F) SEM images of COFs, PCOFs, and ICA@PCOFs; (G) particle size analysis of COFs, PCOFs, and ICA@PCOFs.

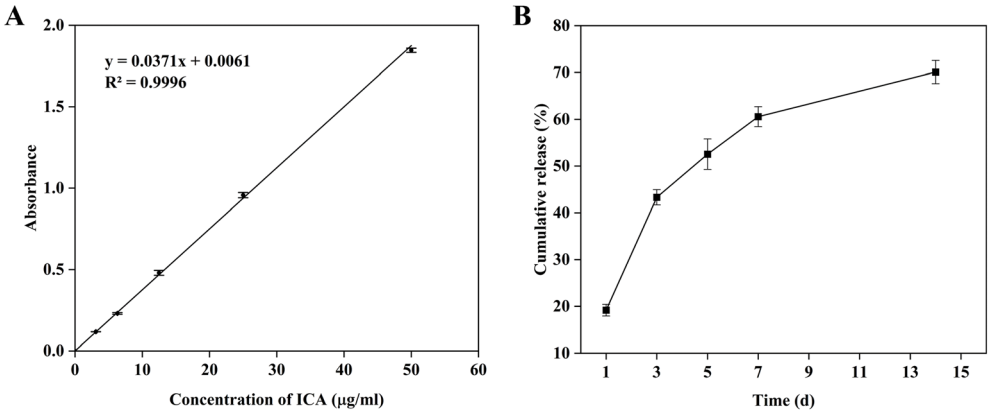

Fig. 3 Evaluation of the drug loading performance of ICA@PCOFs nanoparticles: (A) standard curve of ICA; (B) *in vitro* release profile of ICA in ICA@PCOFs.

results collectively confirm the successful synthesis of ICA@PCOFs nanomaterials.

3.1.2 The drug loading performance of ICA in ICA@PCOFs. The DLC and EE of ICA in ICA@PCOFs was determined based on the standard curve of ICA concentration, as illustrated in Fig. 3A. The standard curve was constructed by measuring the absorbance values of ICA at different concentrations, with the equation derived as $y = 0.0371x + 0.0061$ and an R^2 value of 0.9996, which indicates a strong linear correlation between ICA concentration and absorbance within the tested concentration range. This result suggests that the method used for drug quantification is accurate and reliable.

Based on this standard curve, the average DLC and EE of ICA in ICA@PCOFs was calculated to be 12.35% and 32.90% according to previous publications,[36–38] as shown in Table 1. This value reflects the successful incorporation of ICA into the PCOFs nanostructures, indicating that the PCA@PCOFs can effectively act as a drug carrier. The relatively DLC (12.35%) and EE (32.90%) are consistent with typical results observed in drug-loaded nanomaterials, particularly those based on porous frameworks like COFs, which may have limitations in terms of loading capacity due to the balance between pore size and surface area.[39–41] However, this DLC is still promising and demonstrates the feasibility of utilizing PCOFs for sustained drug delivery applications. The relatively lower DLC compared to some other drug delivery systems could be attributed to the limited pore size of the PCOFs. Although the PCOFs exhibit a significant surface area (930 $m^2 g^{-1}$) and moderate pore size (approximately 2.3 nm), which allows for efficient adsorption and entrapment of molecules, there may be limitations in accommodating larger drug molecules such as ICA. Additionally, the surface modification using PDA may have influenced the porosity and surface characteristics, which could further affect the drug loading capacity.

Table 1 Absorbance, DLC and EE of ICA in ICA@PCOFs nanoparticles

Times	1	2	3	4	5	Average
Absorbance	1.128	1.164	1.138	1.121	1.206	1.151
DLC (%)	12.09	12.49	12.21	12.01	12.94	12.35
EE (%)	32.23	33.28	32.52	32.01	34.47	32.90

Bone tissue repair and regeneration is a prolonged and complex biological process. Sustained drug release throughout the entire healing period—especially during the later stages of osteogenesis—can further enhance bone regeneration.[42] Fig. 3B shows the *in vitro* drug release profile of ICA from ICA@PCOFs. The results indicate that ICA exhibited a rapid release during the first 3 days, reaching a cumulative release of 43.3%. After this initial phase, the release rate slowed down and transitioned into a sustained and stable release pattern. By day 14, the cumulative release reached 70.1%, and the release process was still ongoing. These findings demonstrate that ICA@PCOFs possess excellent controlled and long-term release behavior, enabling sustained therapeutic delivery throughout the extended period required for bone tissue regeneration.

This research demonstrates the potential of ICA@PCOFs as a drug delivery system for bone tissue regeneration, particularly in terms of its ability to provide a controlled release environment. Future work could aim to optimize the drug loading process by exploring modifications to the COFs' pore structure or investigating the use of different types of drug molecules to further enhance the loading capacity.

3.2 Biocompatibility of ICA@PCOFs

ICA@PCOFs, as a bone defect implant material, needs to demonstrate excellent biocompatibility, which is an essential element in tissue engineering.[43,44] In this study, the biocompatibility of ICA@PCOFs nanoparticles was evaluated by co-culturing HBMSCs with extracts at different concentration gradients for 1, 3, and 5 days. The results observed *via* microscopy, as shown in Fig. 4, indicated no significant differences in cell confluence across all groups on day 1. However, as the culture time extended, by day 5, the overall proliferation of HBMSCs showed a downward trend with increasing ICA concentration. Compared to the control group (0 μg mL^{-1}), the low concentration group (1 μg mL^{-1}) exhibited faster cell proliferation, whereas the high concentration group (1000 μg mL^{-1}) showed a slower rate of proliferation. These findings

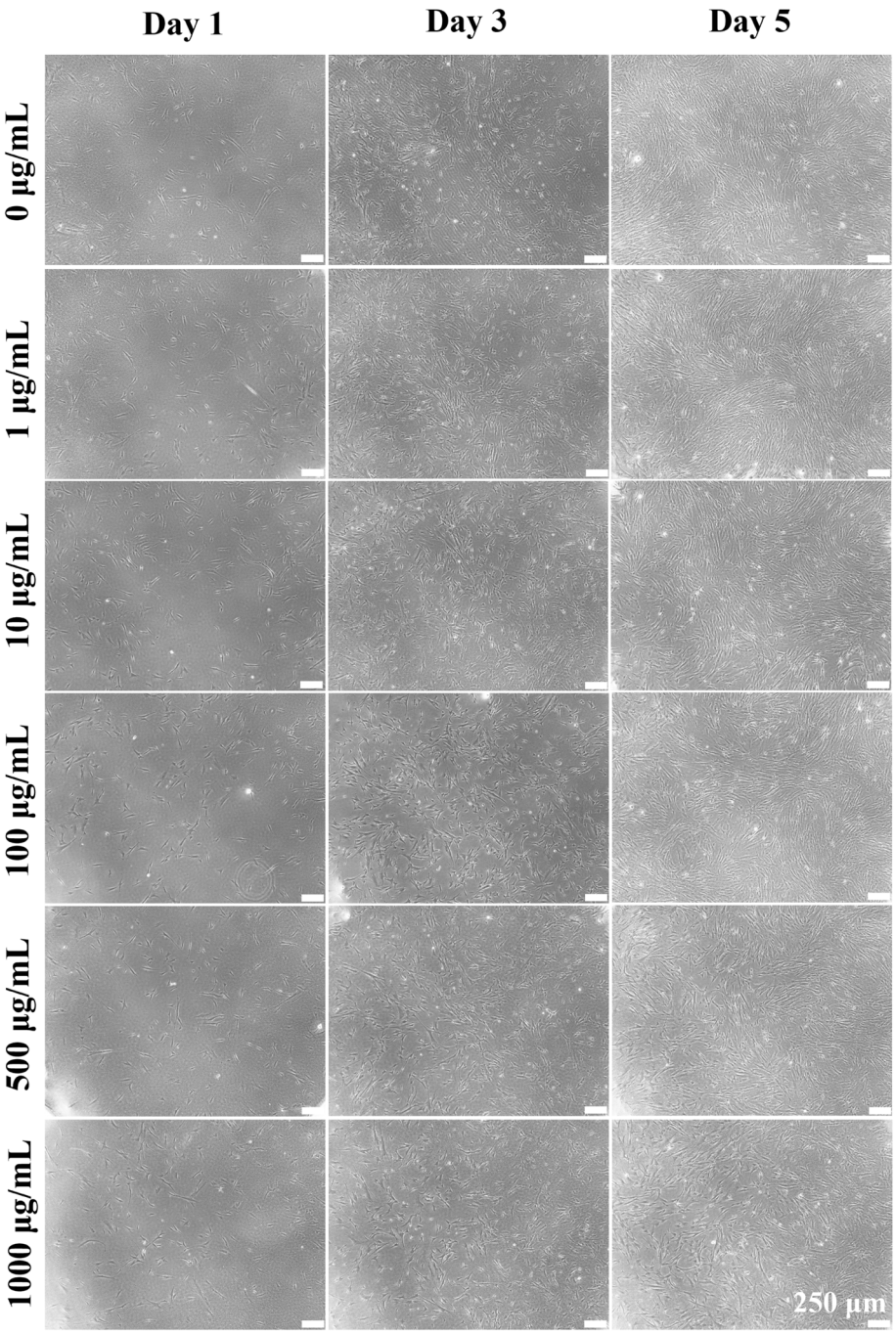

Fig. 4 Phase contrast images of HBMSCs co-cultured with ICA@PCOFs extracts at different concentration gradients.

were further corroborated by the CCK-8 statistical results presented in Fig. 5, which were consistent with the microscopic observations. It was evident that ICA@PCOFs had an inhibitory effect on cell proliferation at higher concentrations, whereas it significantly promoted cell proliferation at lower concentrations, with the most prominent promotion observed at 1 μg mL^{-1}. This result suggests that ICA@PCOFs nanoparticles can serve as an effective and safe material for bone tissue engineering, with the potential to enhance cell proliferation at appropriate concentrations. The biocompatibility of a material is crucial for its application in bone tissue regeneration. The results of this study indicate that ICA@PCOFs can positively influence the proliferation of HBMSCs at low concentrations, while higher concentrations may pose potential cytotoxic effects. This balance between promoting and inhibiting cell proliferation is particularly important when designing implantable materials for tissue engineering, as excessive cytotoxicity could hinder the healing process or lead to implant failure. The observed concentration-dependent effects of ICA@PCOFs may be attributed to the unique properties of the nanoparticles, such as surface modification, pore size, and the release kinetics of the drug. The 1 μg mL^{-1} concentration,

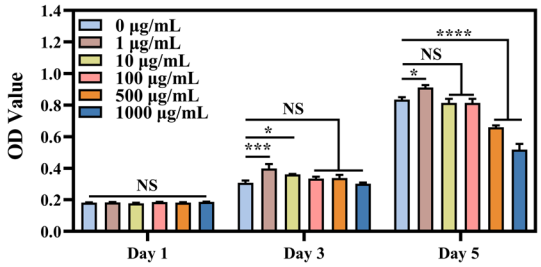

Fig. 5 CCK-8 results of HBMSCs co-cultured with ICA@PCOFs extracts at different concentration gradients. Compared with the 0 μg mL^{-1} group, NS indicates no significant difference; *, $p < 0.05$; ***, $p < 0.001$; ****, $p < 0.0001$. $n = 3$.

which exhibited the best proliferation effect, could potentially represent the optimal balance between bioactivity and biocompatibility, making it a suitable candidate for further investigation in bone regeneration applications. Therefore, the concentration of 1 μg mL^{-1} was selected for the subsequent osteogenesis and anti-inflammatory experiments.

3.3 Immunomodulatory effects of ICA@PCOFs

Macrophages play a critical role in the repair process of bone defects, with their rapid response and polarization shifts being pivotal. Initially, these cells migrate swiftly to the injury site, where they recognize and clear dead cells and tissue debris. In their early phase, they predominantly exhibit an M1 phenotype, actively secreting pro-inflammatory factors such as iNOS, TNF-α, and interleukin-1 (IL-1), which facilitate the activation and differentiation of osteoclasts, intensifying the inflammatory response.[45] This phenomenon is a necessary physiological process during the early phase of lesion clearance. As the repair

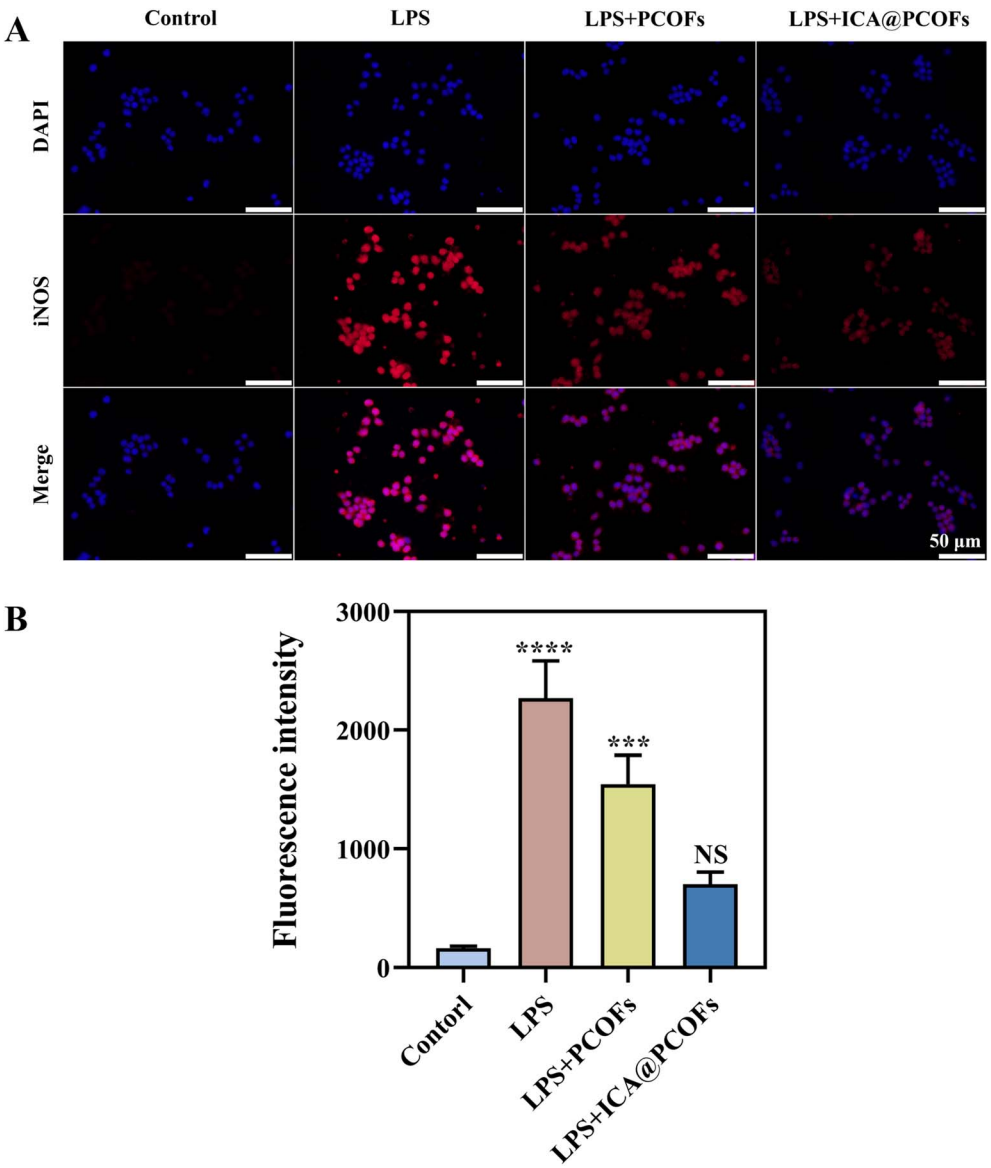

Fig. 6 Immunofluorescent evaluation of iNOS expression in macrophages cultured with PCOFs and ICA@PCOFs extracts *in vitro*: (A) representative immunofluorescent staining images; (B) semi-quantitative analysis of fluorescence intensity. Compared to the control group, NS, no significant difference; ***, $p < 0.001$; ****, $p < 0.0001$. $n = 3$.

process progresses, particularly with the reestablishment of blood supply and the recruitment of mesenchymal stem cells that differentiate into fibroblasts, osteoblasts, and chondrocytes, macrophages gradually transition from the M1 to the M2 phenotype.[46] M2 macrophages, in an improved hypoxic and ischemic microenvironment, help to mitigate inflammation and promote tissue repair and regeneration by releasing anti-inflammatory factors such as CD206, interleukin-10 (IL-10), and transforming growth factor-beta (TGF-β).[47–49] This process fosters the formation of new bone tissue and collagen fibers, effectively filling the tissue defect.[50] Therefore, the proper regulation of macrophage polarization is crucial in the repair of bone defects. This process involves not only a shift from acute inflammatory responses to tissue reconstruction but also the fine regulation of extracellular signals. This study utilized immunofluorescent staining for iNOS and CD206 to mark M1 and M2 macrophages, respectively, assessing the immunomodulatory capabilities of ICA@PCOFs nanoparticles, further validating their potential mechanism in promoting bone defect repair.

Building upon the theoretical framework of macrophage polarization dynamics in bone repair, we experimentally evaluated the immunomodulatory effects of ICA@PCOFs under inflammatory conditions. Immunofluorescence quantification of M1/M2 phenotypic markers provided direct evidence for the nanoparticle-mediated regulation of macrophage behavior. As shown in Fig. 6A, in the control group, the expression of iNOS was almost invisible, exhibiting very low red fluorescence signals. In contrast, the LPS group, used as an inflammation-induced control group, showed a significant enhancement in

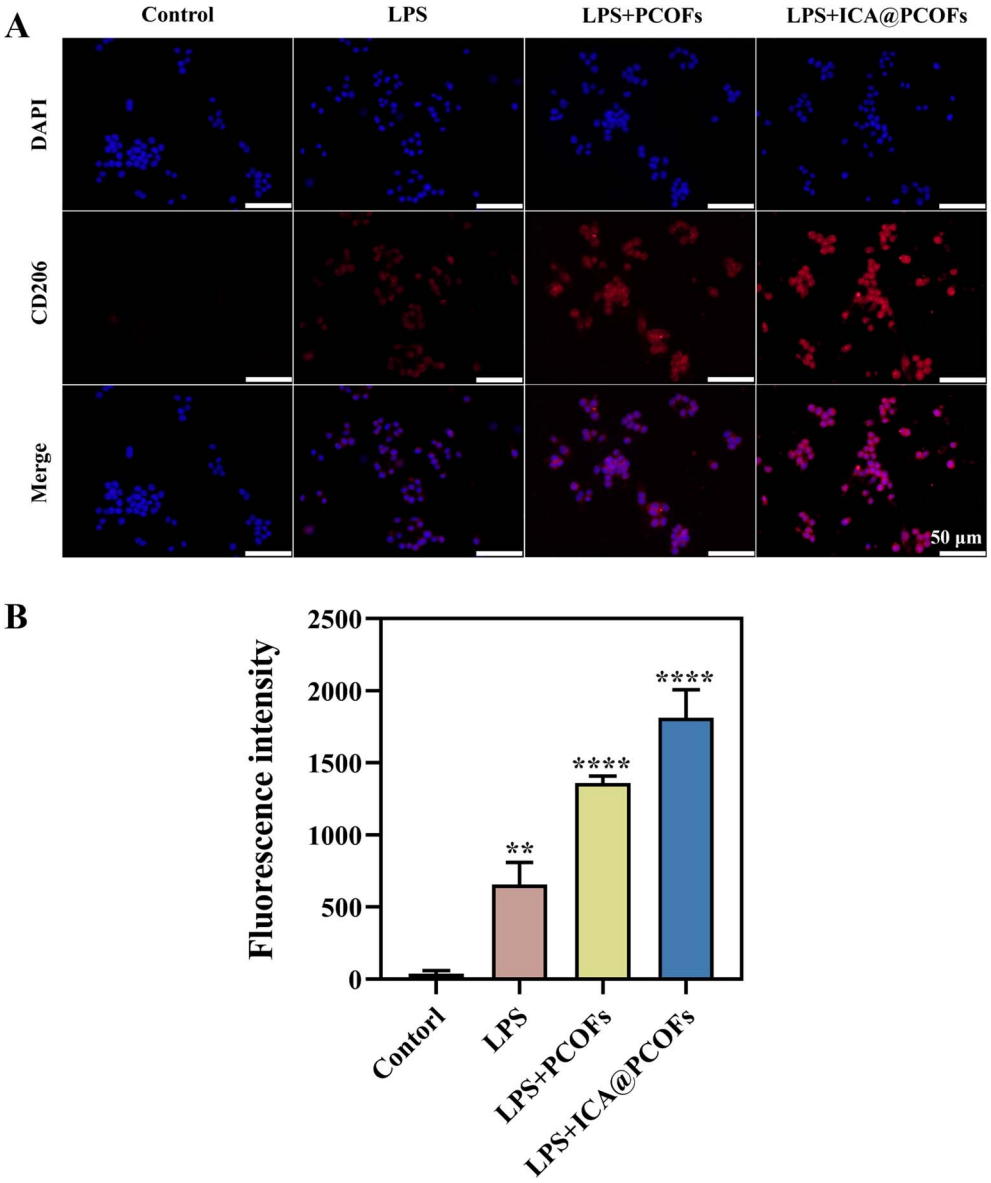

Fig. 7 Immunofluorescent evaluation of CD206 expression in macrophages cultured with PCOFs and ICA@PCOFs extracts *in vitro*: (A) representative immunofluorescent staining images; (B) semi-quantitative analysis of fluorescence intensity. Compared to the control group, **, $p < 0.01$; ****, $p < 0.0001$. $n = 3$.

red fluorescence, indicating high levels of iNOS expression. In the groups treated with PCOFs extract (LPS + PCOFs) and ICA@PCOFs extract (LPS + ICA@PCOFs), a gradual reduction in fluorescence intensity was observed, suggesting a decrease in iNOS expression levels, with the concurrent presence of ICA and PCOFs contributing to the reduction in M1 macrophage generation. This observation was further validated through semi-quantitative fluorescence analysis in Fig. 6B. Compared to the control group, iNOS expression was significantly increased in the LPS group, while it progressively decreased in the LPS + PCOFs and LPS + ICA@PCOFs groups, indicating that PCOFs and ICA@PCOFs effectively suppress the inflammatory response induced by LPS. Moreover, the addition of ICA appeared to further enhance this inhibitory effect, demonstrating stronger immunomodulatory potential in ICA@PCOFs. These results clearly show that COFs nanoparticles, modified with PDA and loaded with ICA, have a significant effect in suppressing the inflammatory environment, particularly in inhibiting the expression of the M1 macrophage marker iNOS. This result confirms the potential application of these materials in biomedical applications, especially in anti-inflammatory therapies.

Complementary to the findings on M1 phenotype suppression, we further interrogated the material's capacity to drive pro-regenerative macrophage polarization. Simultaneous evaluation of M2 marker expression revealed the dual-directional immunomodulatory functionality inherent to the nanocomposite system. Fig. 7A and B further provide the results of CD206 immunofluorescence staining and semi-quantitative analysis for macrophages cultured *in vitro* with PCOFs and ICA@PCOFs extracts. As shown in Fig. 7A, in the control group, CD206 expression is nearly undetectable with very weak fluorescence signaling. In contrast, the LPS-treated group exhibits a slight, faint red fluorescence, indicating minor M2 macrophage activation under inflammatory conditions. However, upon addition of PCOFs and ICA@PCOFs extracts, CD206 expression in both the LPS + PCOFs and LPS + ICA@PCOFs groups progressively increases, as evidenced by the strengthening fluorescence intensity. Semi-quantitative analysis in Fig. 7B of the fluorescence further corroborates these observations. Compared to the control group, CD206 expression is lower in the LPS group, but significantly elevated in the LPS + PCOFs and LPS + ICA@PCOFs groups, suggesting that PCOFs and ICA@PCOFs effectively promote M2 macrophage polarization, thereby enhancing anti-inflammatory responses.

During the process of bone defect repair, controlling the inflammatory response is crucial because excessive inflammation can delay or inhibit bone regeneration. As demonstrated in Fig. 6 and 7, COFs nanomaterials modified with PDA and loaded with ICA effectively suppress the activity of M1 macrophages while significantly enhancing the anti-inflammatory functionality of M2 macrophages, thereby exhibiting

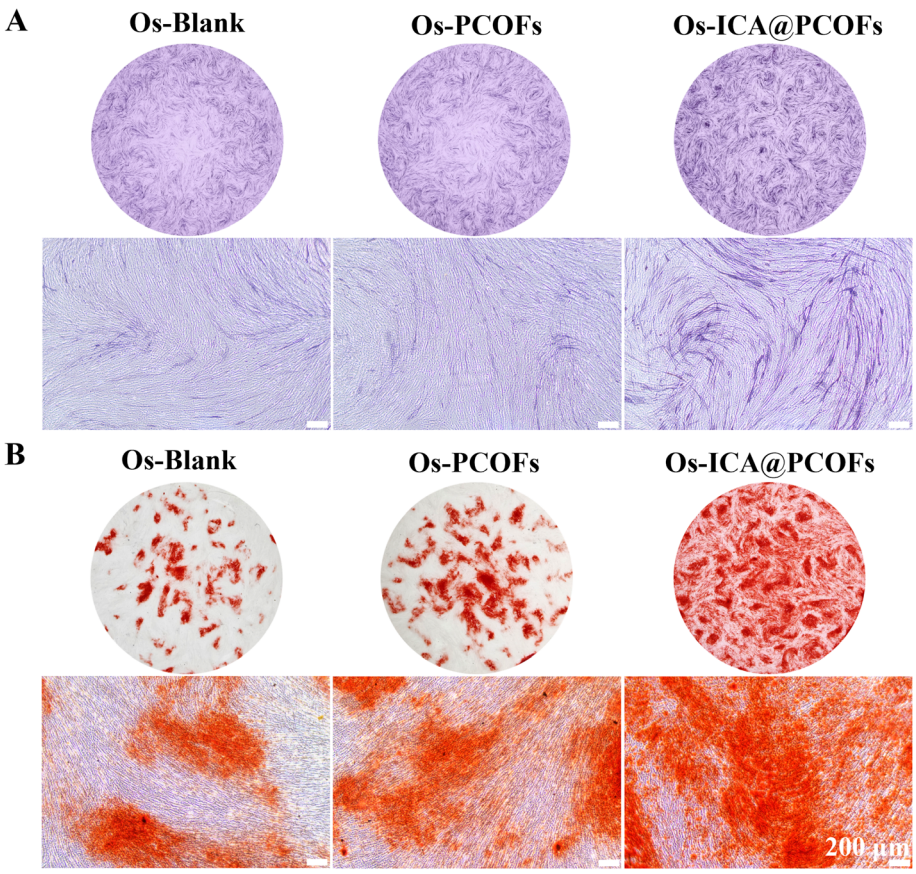

Fig. 8 *In vitro* evaluation of osteogenic differentiation in HBMSCs treated with extracts from the Os-Blank, Os-PCOFs, and Os-ICA@PCOFs groups: (A) ALP staining at day 7; (B) ARS staining at day 14.

substantial anti-inflammatory effects. This immunomodulatory action is particularly suitable for bone defect repair as it can effectively reduce inflammation-mediated bone tissue damage and promote the regeneration of healthy bone tissue.

These experimental results align with the documented effects of PDA and ICA on immunomodulation in the literature, highlighting the potential application of these materials in regulating inflammatory responses and facilitating inflammation resolution mechanisms, especially in the field of bone defect repair.[51–54]

3.4 Osteogenesis of ICA@PCOFs

ALP is a key marker of the early stages of osteogenesis, primarily located in the cell membrane's binding transport proteins, facilitating the maturation and calcification of osteoblasts.[55] ARS staining is a commonly used method to stain the calcium content in cells and is an important indicator for assessing the differentiation and maturation of osteoblasts.[56] Therefore, this study employs ALP and ARS staining to evaluate the effect of ICA@PCOFs extract on the osteogenic differentiation of HBMSCs.

To investigate the temporal progression of osteogenic differentiation induced by ICA@PCOFs, we analyzed ALP

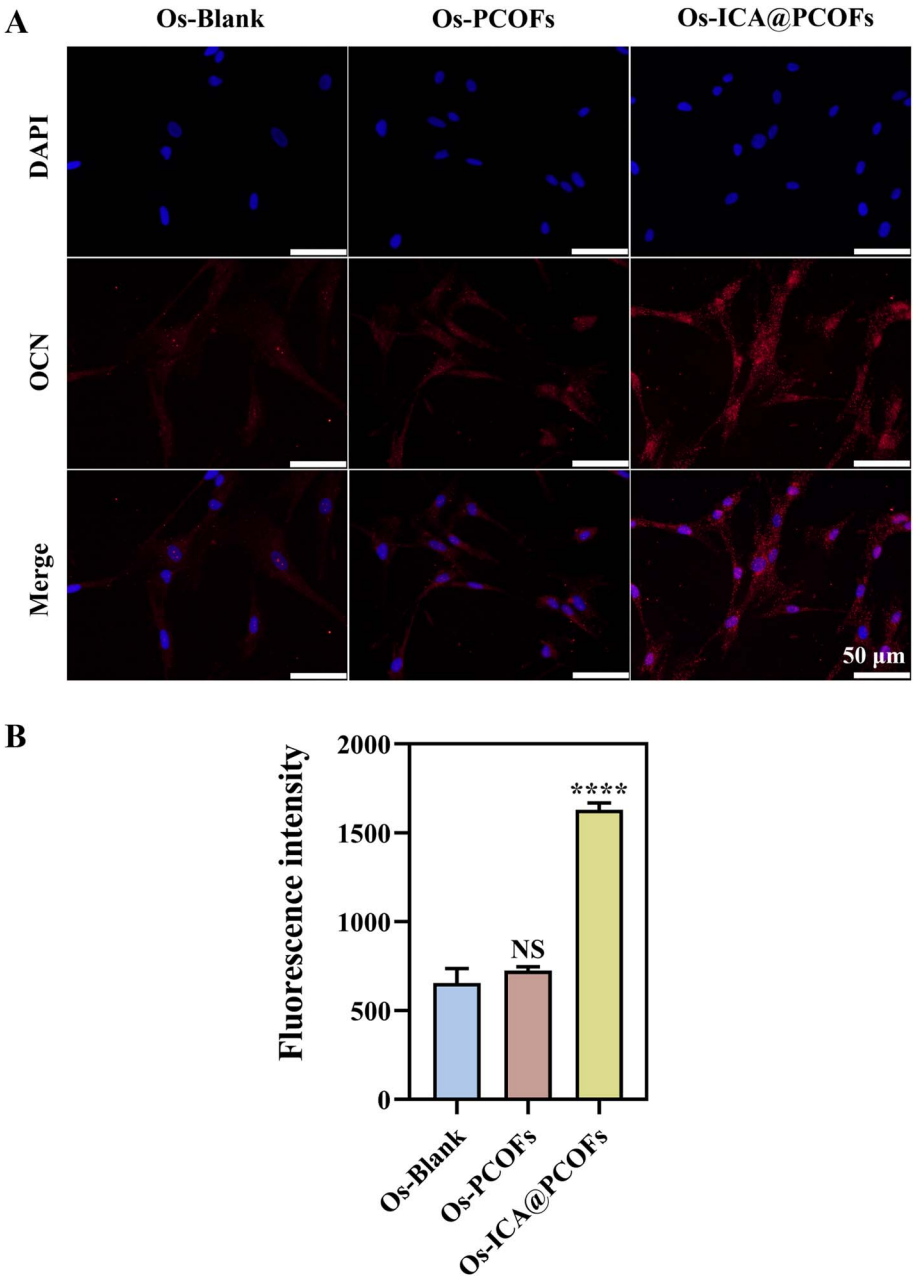

Fig. 9 Immunofluorescent evaluation of OCN expression in HBMSCs treated with extracts from the Os-Blank, Os-PCOFs, and Os-ICA@PCOFs groups: (A) OCN immunofluorescence staining; (B) semi-quantitative analysis of fluorescence intensity. Compared with the Os-Blank group, NS: no significant difference; ****, $p < 0.0001$. $n = 3$.

activity at 7 days and calcium deposition at 14 days. Sequential assessment of these markers allowed us to capture both early differentiation events and subsequent mineralization processes. Fig. 8A and B present the results of ALP staining at 7 days and ARS staining at 14 days. The ALP staining results show that both the Os-Blank group and the Os-PCOFs group exhibit faint staining, with no significant differences between them, indicating that PCOFs do not significantly promote osteogenic differentiation in HBMSCs. In contrast, the Os-ICA@PCOFs group shows noticeably darker staining, indicating that the addition of ICA significantly promotes the osteogenic differentiation of HBMSCs. The ARS staining results at 14 days further confirm this trend. Only a small number of red mineralized nodules are observed in the Os-Blank and Os-PCOFs groups, with these nodules being sparsely distributed. In contrast, the Os-ICA@PCOFs group shows a significantly higher density of red mineralized nodules, which are tightly clustered and more extensively distributed. Therefore, Os-ICA@PCOFs, by continuously releasing ICA, can effectively activate the osteogenic biological pathways in HBMSCs. These results not only significantly promote early osteogenic differentiation in stem cells but also enhance the formation of mineralized nodules during the mineralization process, thus improving the capacity for bone tissue regeneration.

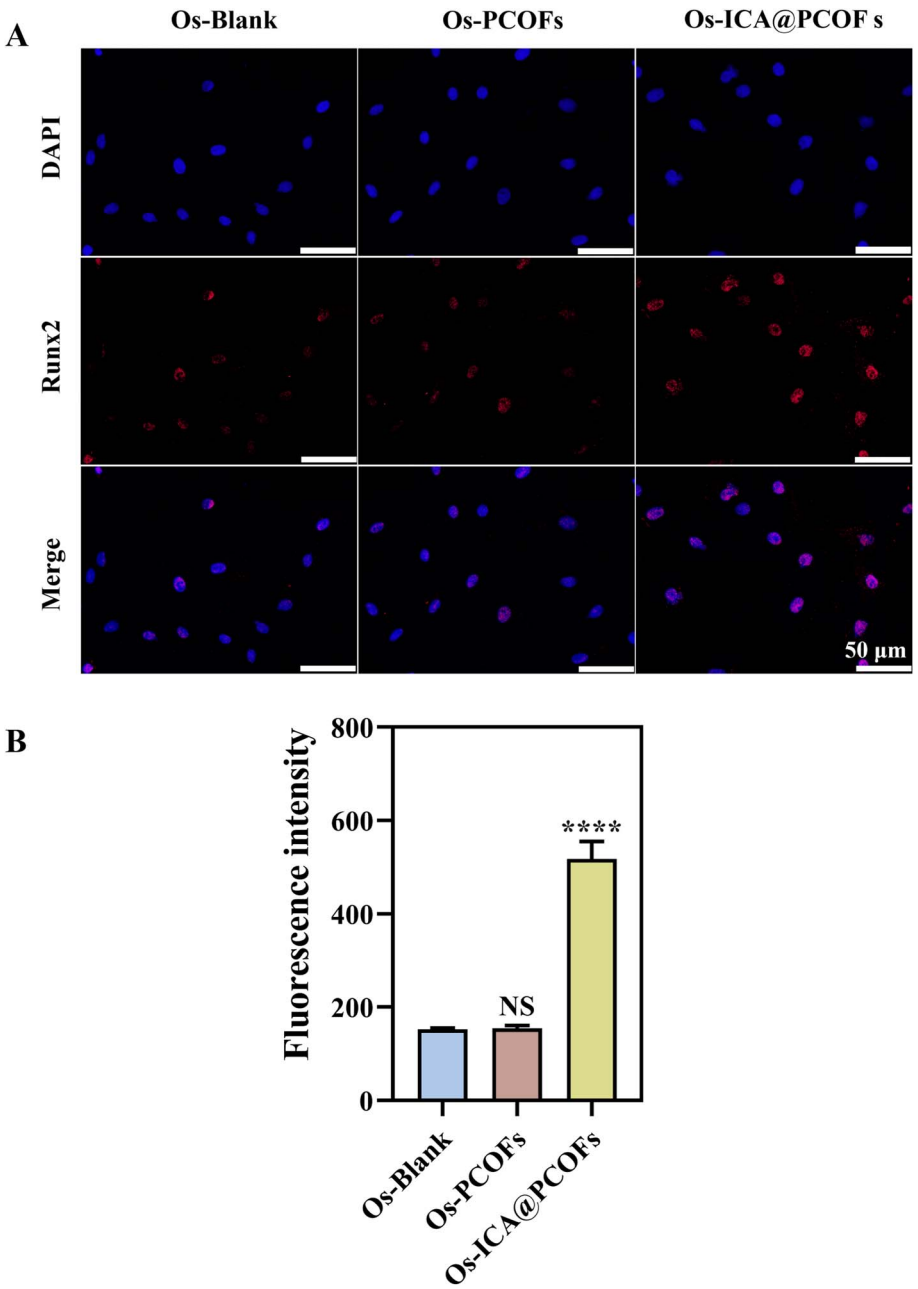

Fig. 10 Immunofluorescent evaluation of Runx2 expression in HBMSCs treated with extracts from the Os-Blank, Os-PCOFs, and Os-ICA@PCOFs groups: (A) Runx2 immunofluorescence staining; (B) semi-quantitative analysis of fluorescence intensity. Compared with the Os-Blank group, NS: no significant difference; ****, $p < 0.0001$. $n = 3$.

Runx2 plays a critical role in osteogenic differentiation by influencing the expression of bone-specific matrix protein genes.[57] OCN is a calcium-binding protein predominantly synthesized by osteoblasts and plays a crucial role in regulating bone calcium metabolism.[58] Therefore, this study further evaluates the effect of ICA@PCOFs extract on osteogenic differentiation of HBMSCs by detecting the expression of OCN and Runx2 proteins using immunofluorescence techniques.

Having established the regulatory role of ICA@PCOFs on osteogenic transcription factors, we next examined their functional impact on bone matrix maturation. Immunofluorescence quantification of osteocalcin (OCN), a late-stage mineralization marker, revealed the material's capacity to drive terminal osteoblast differentiation. From the results shown in Fig. 9A, it can be observed that the overall red fluorescence intensity in the Os-PCOFs group exhibited no significant difference compared to the Os-Blank group, indicating that PCOFs without ICA loading had a limited effect on osteogenic differentiation. Thus, PCOFs alone do not significantly influence the osteogenic activity of HBMSCs. However, in the Os-ICA@PCOFs group, the cells exhibited much stronger red fluorescence, demonstrating that the incorporation of ICA significantly upregulated the expression of OCN. The fluorescence semi-quantitative analysis in Fig. 9B further confirmed this trend, providing additional evidence that ICA-loaded nanomaterials exert a positive effect on osteogenic activity.

To comprehensively assess the upstream molecular mechanisms underlying this osteoinductive effect, we focused on Runx2 nuclear translocation—a master regulatory event initiating osteoblast lineage commitment. Spatial resolution of Runx2 subcellular localization provided critical insights into the nanomaterial's early-stage differentiation control. The immunofluorescence results for Runx2 in Fig. 10A and B further support this conclusion. In the Os-Blank and Os-PCOFs groups, the red fluorescence intensity in the nuclear region was relatively weak, indicating a low expression level of Runx2. This result suggests that PCOFs without ICA loading did not significantly affect the nuclear localization and expression of Runx2. In contrast, the Os-ICA@PCOFs group exhibited a markedly stronger red fluorescence signal in the nuclear region, and semi-quantitative analysis further confirmed this trend, demonstrating that ICA loading significantly enhanced the nuclear localization and expression of Runx2, thereby driving osteogenic differentiation.

These results further validate that ICA@PCOFs nanomaterials effectively enhance the osteogenic differentiation of HBMSCs by promoting the nuclear expression of Runx2 while simultaneously upregulating the synthesis of the late-stage osteogenic marker protein OCN. The osteogenic-promoting effect of ICA-loaded nanomaterials may be attributed to their regulation of bone formation-related signaling pathways, promotion of osteogenic cell phenotype transition, and enhancement of bone matrix deposition. Moreover, these findings highlight the potential application of ICA in bone tissue engineering materials, providing novel insights and strategies for bone defect repair. Future studies should further investigate the *in vivo* osteogenic effects and underlying molecular mechanisms of ICA@PCOFs to facilitate the clinical translation of this material in bone regeneration medicine.

4. Conclusion

This study successfully developed an ICA delivery system based on COFs and systematically evaluated its dual role in immune modulation and osteogenic differentiation. COF nanoparticles were synthesized at room temperature and further modified with PDA to obtain PCOFs. Leveraging the strong adhesive properties of PDA, ICA was effectively loaded onto the surface of PCOFs, forming a stable ICA@PCOFs nanocomposite. A series of characterization techniques, including SEM, FTIR, and TGA, confirmed the successful synthesis and stability of ICA@PCOFs. In *in vitro* biological evaluations, the CCK-8 assay was employed to determine the optimal concentration, ensuring cell compatibility and experimental reliability. Subsequently, immunofluorescence staining and osteogenic differentiation assays demonstrated that ICA@PCOFs effectively regulated macrophage polarization, significantly inhibiting the expression of M1 pro-inflammatory macrophages (iNOS+) while promoting M2 anti-inflammatory macrophages (CD206+), indicating its potent immunomodulatory capabilities. Furthermore, ICA@PCOFs significantly enhanced osteogenic differentiation, as evidenced by increased ALP activity, enhanced mineralized nodule formation (ARS staining), and upregulated expression of key osteogenic markers (OCN, Runx2), as well as increased protein expression of osteogenic markers (OCN+ and Runx2+ cells), confirming its superior osteogenesis-promoting effects. Overall, ICA@PCOFs improved the local inflammatory microenvironment through immune modulation and accelerated bone tissue regeneration by promoting osteogenic differentiation, demonstrating great potential in bone defect repair. This study not only provides a novel research direction for COFs-based nanomaterials in bone tissue engineering but also presents a promising strategy for localized ICA delivery. Future studies will further explore the *in vivo* bone regeneration efficacy and clinical translational potential of ICA@PCOFs in animal models, aiming to offer a safer and more effective therapeutic approach for bone tissue regeneration.

Data availability

The authors affirm that the data supporting the findings of this study are included in the article, additional data can be made available from the corresponding author upon reasonable request.

Author contributions

Mingdong Luo, Xiaorong Lan, Zhoukun He, and Shiting Li contributed to the experimental design and conceptualization. Mingdong Luo, Xueqing Lin, and Qishan Xie performed the experiments and drafted the manuscript. Mingdong Luo, Xueqing Lin, Na Wang, Qishan Xie, and Shiyi Zeng were responsible for data collection, analysis, and statistical evaluation. Xiaorong Lan, Zhoukun He, and Shiting Li reviewed and

revised the manuscript, providing critical feedback and guidance for its finalization.

Conflicts of interest

The authors declare no conflict of interest.

Acknowledgements

The authors would like to acknowledge the financial support from the Sichuan Science and Technology Program (No. 2024NSFSC0246), the Luzhou Science and Technology Program (No. 2022-GYF-12), the Stomatology Key Program of Southwest Medical University in 2024 (No. 2024KQZX01), the Innovative Leading Talents Program of The Affiliated Stomatological Hospital of Southwest Medical University (No. 2022LJ02), and the Talent Introduction Program of The Affiliated Stomatological Hospital of Southwest Medical University (No. 2022BS02).

References

1 A. S. Greenwald, S. D. Boden, V. M. Goldberg, *et al.*, Bone-graft substitutes: facts, fictions, and applications, *J. Bone Jt. Surg., Am. Vol.*, 2001, **83**(2), 98–103.
2 Research G V, Bone Grafts And Substitutes Market Size, Share & Trends Analysis Report By Material Type (Allograft, Synthetic), By Application (Spinal Fusion, Dental), By Region, And Segment Forecasts, 2025–2030, *Grand View Research: Grand View Research*, 2024.
3 W. Yu, S. Li, X. Guan, *et al.*, Higher yield and enhanced therapeutic effects of exosomes derived from MSCs in hydrogel-assisted 3D culture system for bone regeneration, *Biomater. Adv.*, 2022, **133**, 112646.
4 A. Stahl and Y. P. Yang, Regenerative Approaches for the Treatment of Large Bone Defects, *Tissue Eng., Part B*, 2021, **27**(6), 539–547.
5 S. Li, L. Zhang, C. Liu, *et al.*, Spontaneous immunomodulation and regulation of angiogenesis and osteogenesis by Sr/Cu-borosilicate glass (BSG) bone cement to repair critical bone defects, *Bioact. Mater.*, 2023, **23**, 101–117.
6 L. Gu, R. Huang, N. Ni, *et al.*, Advances and Prospects in Materials for Craniofacial Bone Reconstruction, *ACS Biomater. Sci. Eng.*, 2023, **9**(8), 4462–4496.
7 R. Shen and J. H. Wang, The effect of icariin on immunity and its potential application, *Am. J. Clin. Exp. Immunol.*, 2018, **7**(3), 50–56.
8 L. Bai, Y. Liu, X. Zhang, *et al.*, Osteoporosis remission *via* an anti-inflammaging effect by icariin activated autophagy, *Biomaterials*, 2023, 297.
9 T. Song, J. Yang, P. Liu, *et al.*, Icariin self-crosslinked network functionalized strontium-doped bioceramic scaffolds synergistically enhanced the healing of osteoporotic bone defects, *Composites, Part B*, 2022, 235.
10 H. Zhou, Y. Yuan, Y. Liu, *et al.*, Icariin protects H9c2 cardiomyocytes from lipopolysaccharide-induced injury *via* inhibition of the reactive oxygen species-dependent c-Jun N-terminal kinases/nuclear factor-κB pathway, *Mol. Med. Rep.*, 2015, **11**(6), 4327–4332.
11 Z. Luo, J. Dong and J. Wu, Impact of Icariin and its derivatives on inflammatory diseases and relevant signaling pathways, *Int. Immunopharmacol.*, 2022, **108**, 108861.
12 A. Khodaei, Q. Nawaz, Z. Zhu, *et al.*, Biomolecule and Ion Releasing Mesoporous Nanoparticles: Nonconvergent Osteogenic and Osteo-immunogenic Performance, *ACS Appl. Mater. Interfaces*, 2024, **16**(49), 67491–67503.
13 A. Yang, C. Yu, Q. Lu, *et al.*, Mechanism of Action of Icariin in Bone Marrow Mesenchymal Stem Cells, *Stem Cells Int.*, 2019, **2019**, 5747298.
14 F. Wang, Z. Yang, W. He, *et al.*, Effects of icariin on the proliferation and osteogenic differentiation of human amniotic mesenchymal stem cells, *J. Orthop. Surg. Res.*, 2020, **15**(1), 578.
15 Q. Wei, J. Zhang, G. Hong, *et al.*, Icariin promotes osteogenic differentiation of rat bone marrow stromal cells by activating the ERα-Wnt/β-catenin signaling pathway, *Biomed. Pharmacother.*, 2016, **84**, 931–939.
16 C. C. Poon, C. Au-Yeung, K. Y. Wong, *et al.*, Icariin promotes cell adhesion for osteogenesis in bone marrow stromal cells *via* binding to integrin α5β1, *Phytomedicine*, 2024, **133**, 155887.
17 J. Tan, Z. Chen, Z. Xu, *et al.*, Small intestine submucosa decorated 3D printed scaffold accelerated diabetic bone regeneration by ameliorating the microenvironment, *J. Mater. Chem. B*, 2024, **12**(37), 9375–9389.
18 H. Li, Q. Pan, Y. Ma, *et al.*, Three-Dimensional Covalent Organic Frameworks with Dual Linkages for Bifunctional Cascade Catalysis, *J. Am. Chem. Soc.*, 2016, **138**(44), 14783–14788.
19 J. Li, X. Jing, Q. Li, *et al.*, Bulk COFs and COF nanosheets for electrochemical energy storage and conversion, *Chem. Soc. Rev.*, 2020, **49**(11), 3565–3604.
20 A. P. Côté, A. I. Benin, N. W. Ockwig, *et al.*, Porous, crystalline, covalent organic frameworks, *Science*, 2005, **310**(5751), 1166–1170.
21 S. Kandambeth, A. Mallick, B. Lukose, *et al.*, Construction of crystalline 2D covalent organic frameworks with remarkable chemical (acid/base) stability *via* a combined reversible and irreversible route, *J. Am. Chem. Soc.*, 2012, **134**(48), 19524–19527.
22 R. Liu, K. T. Tan, Y. Gong, *et al.*, Covalent organic frameworks: an ideal platform for designing ordered materials and advanced applications, *Chem. Soc. Rev.*, 2021, **50**(1), 120–242.
23 S. Bhunia, M. K. Jaiswal, K. A. Singh, *et al.*, 2D Covalent Organic Framework Direct Osteogenic Differentiation of Stem Cells, *Adv. Healthcare Mater.*, 2022, **11**(10), e2101737.
24 H. Li, Y. Jia, S. Bai, *et al.*, Metal-chelated polydopamine nanomaterials: nanoarchitectonics and applications in biomedicine, catalysis, and energy storage, *Adv. Colloid Interface Sci.*, 2024, **334**, 103316.

25 Y. Wu, S. Huo, S. Liu, *et al.*, Cu-Sr Bilayer Bioactive Glass Nanoparticles/Polydopamine Functionalized Polyetheretherketone Enhances Osteogenic Activity and Prevents Implant-Associated Infections through Spatiotemporal Immunomodulation, *Adv. Healthcare Mater.*, 2023, **12**(32), e2301772.
26 C. Qi, L.-H. Fu, H. Xu, *et al.*, Melanin/polydopamine-based nanomaterials for biomedical applications, *Sci. China:Chem.*, 2019, **62**(2), 162–188.
27 J. Du, Y. Zhou, X. Bao, *et al.*, Surface polydopamine modification of bone defect repair materials: characteristics and applications, *Front. Bioeng. Biotechnol.*, 2022, **10**, 974533.
28 S. Liu, C. Hu, Y. Liu, *et al.*, One-Pot Synthesis of DOX@Covalent Organic Framework with Enhanced Chemotherapeutic Efficacy, *Chemistry*, 2019, **25**(17), 4315–4319.
29 H. Xu, J. Gao and D. Jiang, Stable, crystalline, porous, covalent organic frameworks as a platform for chiral organocatalysts, *Nat. Chem.*, 2015, **7**(11), 905–912.
30 X. Shi, Y. Yao, Y. Xu, *et al.*, Imparting Catalytic Activity to a Covalent Organic Framework Material by Nanoparticle Encapsulation, *ACS Appl. Mater. Interfaces*, 2017, **9**(8), 7481–7488.
31 S. Zhou, Y. Kuang, Y. Shi, *et al.*, Modulated covalent organic frameworks with higher specific surface area for the ultrasensitive detection of polybrominated biphenyls, *Chem. Eng. J.*, 2023, 453.
32 S. Roy and J. W. Rhim, Preparation of carrageenan-based functional nanocomposite films incorporated with melanin nanoparticles, *Colloids Surf. B Biointerfaces*, 2019, **176**, 317–324.
33 J. Yu, D. Wei, S. Li, *et al.*, High-performance multifunctional polyvinyl alcohol/starch based active packaging films compatibilized with bioinspired polydopamine nanoparticles, *Int. J. Biol. Macromol.*, 2022, **210**, 654–662.
34 X. Xie, J. Tang, Y. Xing, *et al.*, Intervention of Polydopamine Assembly and Adhesion on Nanoscale Interfaces: State-of-the-Art Designs and Biomedical Applications, *Adv. Healthcare Mater.*, 2021, **10**(9), e2002138.
35 G. P. Chethankumara, K. Nagaraj, V. Krishna and G. Krishnaswamy, Isolation, characterization and *in vitro* cytotoxicity studies of bioactive compounds from *Alseodaphne semecarpifolia* Nees, *Heliyon*, 2021, **7**(6), e07325.
36 A. Das, P. Sengupta, S. Chatterjee, *et al.*, Development and Evaluation of Magnetite Loaded Alginate Beads Based Nanocomposite for Enhanced Targeted Analgesic Drug Delivery, *Magnetochemistry*, 2025, **11**(2), 14.
37 K. Ghosal, S. Adak, C. Agatemor, *et al.*, Novel interpenetrating polymeric network based microbeads for delivery of poorly water soluble drug, *J. Polym. Res.*, 2020, **27**(4), 98.
38 P. Sengupta, A. Das, J. Khanam, *et al.*, Evaluating the potential of ethyl cellulose/eudragit-based griseofulvin loaded nanosponge matrix for topical antifungal drug delivery in a sustained release pattern, *Int. J. Biol. Macromol.*, 2024, 276.
39 G. Zhang, X. Li, Q. Liao, *et al.*, Water-dispersible PEG-curcumin/amine-functionalized covalent organic framework nanocomposites as smart carriers for *in vivo* drug delivery, *Nat. Commun.*, 2018, **9**(1), 2785.
40 S. Das, T. Sekine, H. Mabuchi, *et al.*, Three-Dimensional Covalent Organic Framework with scu-c Topology for Drug Delivery, *ACS Appl. Mater. Interfaces*, 2022, **14**(42), 48045–48051.
41 W. Ji, P. Zhang, G. Feng, *et al.*, Synthesis of a covalent organic framework with hetero-environmental pores and its medicine co-delivery application, *Nat. Commun.*, 2023, **14**(1), 6049.
42 J. Jiang, C. Cai, S. Li, *et al.*, Triple-effect strategy with taxifolin-whitlockite nanoparticles embedded hydrogel for osteoporotic bone defect repair and bone homeostasis modulation, *Chem. Eng. J.*, 2025, 515.
43 C. Wang, W. Huang, Y. Zhou, *et al.*, 3D printing of bone tissue engineering scaffolds, *Bioact. Mater.*, 2020, **5**(1), 82–91.
44 Z. U. Arif, M. Y. Khalid, R. Noroozi, *et al.*, Additive manufacturing of sustainable biomaterials for biomedical applications, *Asian J. Pharm. Sci.*, 2023, **18**(3), 100812.
45 G. Zhu, T. Zhang, M. Chen, *et al.*, Bone physiological microenvironment and healing mechanism: basis for future bone-tissue engineering scaffolds, *Bioact. Mater.*, 2021, **6**(11), 4110–4140.
46 H. ElHawary, A. Baradaran, J. Abi-Rafeh, *et al.*, Bone Healing and Inflammation: Principles of Fracture and Repair, *Semin. Plast. Surg.*, 2021, **35**(3), 198–203.
47 T. Hou, T. Wang, W. Mu, *et al.*, Nanoparticle-Loaded Polarized-Macrophages for Enhanced Tumor Targeting and Cell-Chemotherapy, *Nano-Micro Lett.*, 2020, **13**(1), 6.
48 K. Ishida, T. Nagatake, A. Saika, *et al.*, Induction of unique macrophage subset by simultaneous stimulation with LPS and IL-4, *Front. Immunol.*, 2023, **14**, 1111729.
49 J. Zhang, X. Liu, C. Wan, *et al.*, NLRP3 inflammasome mediates M1 macrophage polarization and IL-1β production in inflammatory root resorption, *J. Clin. Periodontol.*, 2020, **47**(4), 451–460.
50 A. Salhotra, H. N. Shah, B. Levi and M. T. Longaker, Mechanisms of bone development and repair, *Nat. Rev. Mol. Cell Biol.*, 2020, **21**(11), 696–711.
51 B. Kim, K. Y. Lee and B. Park, Icariin abrogates osteoclast formation through the regulation of the RANKL-mediated TRAF6/NF-κB/ERK signaling pathway in Raw264.7 cells, *Phytomedicine*, 2018, **51**, 181–190.
52 W. Wang, Y. Xiong, R. Zhao, *et al.*, A novel hierarchical biofunctionalized 3D-printed porous Ti6Al4V scaffold with enhanced osteoporotic osseointegration through osteoimmunomodulation, *J. Nanobiotechnol.*, 2022, **20**(1), 68.
53 J. Li, J. Wu, L. Zhu, *et al.*, Polydopamine-coated bioactive glass for immunomodulation and odontogenesis in pulpitis, *Mater. Today Bio*, 2024, **27**, 101130.
54 P. Wu, L. Shen, H. F. Liu, *et al.*, The marriage of immunomodulatory, angiogenic, and osteogenic

capabilities in a piezoelectric hydrogel tissue engineering scaffold for military medicine, *Mil. Med. Res.*, 2023, **10**(1), 35.

55 X. Qi, J. Zhang, H. Yuan, *et al.*, Exosomes Secreted by Human-Induced Pluripotent Stem Cell-Derived Mesenchymal Stem Cells Repair Critical-Sized Bone Defects through Enhanced Angiogenesis and Osteogenesis in Osteoporotic Rats, *Int. J. Biol. Sci.*, 2016, **12**(7), 836–849.

56 R. Ravichandran, J. R. Venugopal, S. Sundarrajan, *et al.*, Precipitation of nanohydroxyapatite on PLLA/PBLG/ collagen nanofibrous structures for the differentiation of adipose derived stem cells to osteogenic lineage, *Biomaterials*, 2012, **33**(3), 846–855.

57 C. P. Yan, X. K. Wang, K. Jiang, *et al.*, β-Ecdysterone Enhanced Bone Regeneration Through the BMP-2/SMAD/ RUNX2/Osterix Signaling Pathway, *Front. Cell Dev. Biol.*, 2022, **10**, 883228.

58 T. Komori, Functions of Osteocalcin in Bone, Pancreas, Testis, and Muscle, *Int. J. Mol. Sci.*, 2020, **21**(20), 7513.